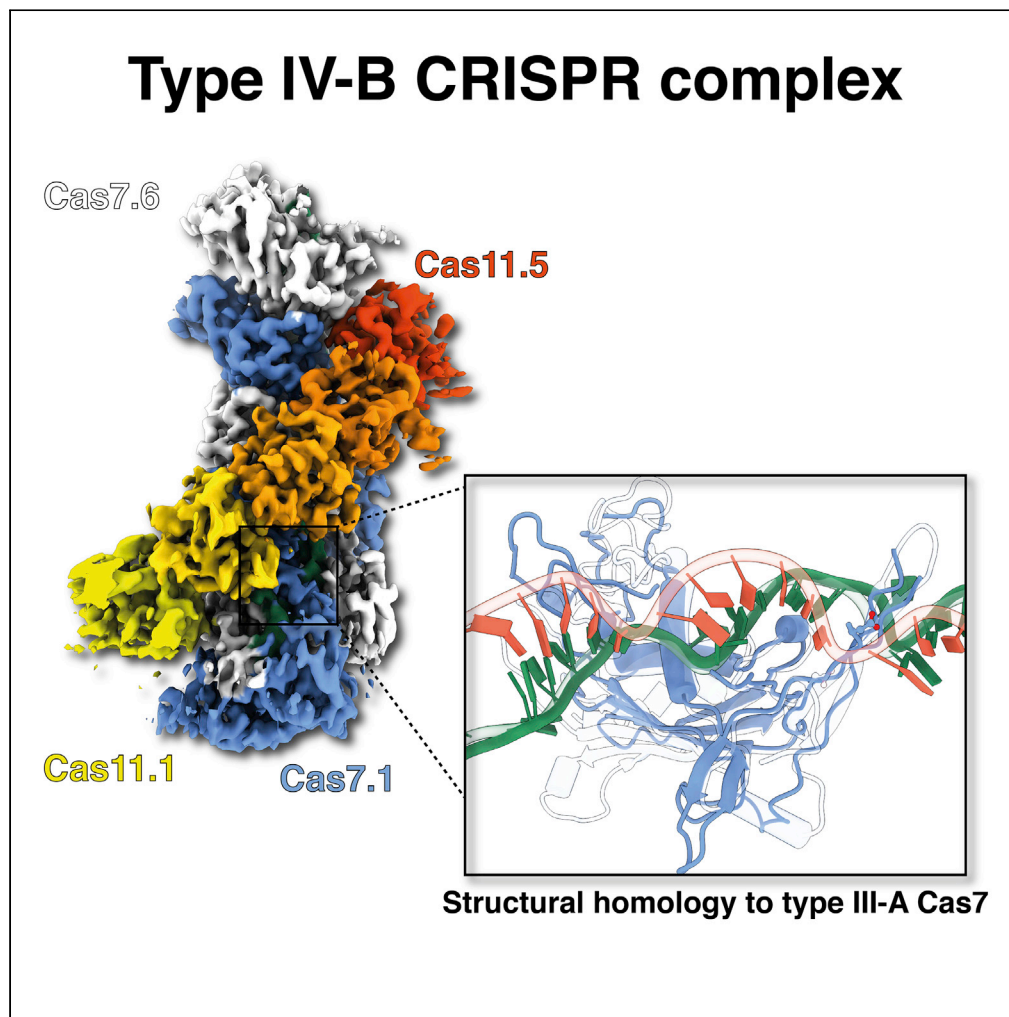


Article

Structure of a type IV CRISPR-Cas
ribonucleoprotein complex

Yi Zhou, Jack P.K. Bravo, Hannah N. Taylor, Jurre A. Steens, Ryan N. Jackson, Raymond H.J. Staals, David W. Taylor

ryan.jackson@usu.edu (R.N.J.)
raymond.staals@wur.nl
(R.H.J.S.)
dtaylor@utexas.edu (D.W.T.)

HIGHLIGHTS

The type IV-B CRISPR-Cas
Csf proteins assemble
around an RNA

First structure of a type IV-
B CRISPR-Cas RNP
complex

Structure confirms
evolutionary link of type IV
systems from a type III-like
ancestor

Assembly of RNP complex
on non-CRISPR RNAs
suggests a non-canonical
role

Zhou et al., iScience 24,
102201
March 19, 2021 © 2021 The
Author(s).
[https://doi.org/10.1016/
j.isci.2021.102201](https://doi.org/10.1016/j.isci.2021.102201)

Article

Structure of a type IV CRISPR-Cas ribonucleoprotein complex

Yi Zhou,^{1,7} Jack P.K. Bravo,^{1,7} Hannah N. Taylor,^{2,7} Jurre A. Steens,³ Ryan N. Jackson,^{2,*} Raymond H.J. Staals,^{3,*} and David W. Taylor^{1,4,5,6,8,*}

SUMMARY

We reveal the cryo-electron microscopy structure of a type IV-B CRISPR ribonucleoprotein (RNP) complex (Csf) at 3.9-Å resolution. The complex best resembles the type III-A CRISPR Csm effector complex, consisting of a Cas7-like (Csf2) filament intertwined with a small subunit (Cas11) filament, but the complex lacks subunits for RNA processing and target DNA cleavage. Surprisingly, instead of assembling around a CRISPR-derived RNA (crRNA), the complex assembles upon heterogeneous RNA of a regular length arranged in a pseudo-A-form configuration. These findings provide a high-resolution glimpse into the assembly and function of enigmatic type IV CRISPR systems, expanding our understanding of class I CRISPR-Cas system architecture, and suggesting a function for type IV-B RNPs that may be distinct from other class 1 CRISPR-associated systems.

INTRODUCTION

Bacteria and archaea employ CRISPR (Clustered Regularly Interspaced Short Palindromic Repeat)-Cas (CRISPR-associated) systems for adaptive immunity against phages, plasmids and other mobile-genetic elements (Makarova et al., 2020). In the multi-subunit class 1 systems, the CRISPR locus is transcribed and processed into small crRNA guides (CRISPR-derived RNA), around which several Cas proteins assemble to form large ribonucleoprotein (RNP) complexes that facilitate RNA-guided surveillance and degradation of complementary targets (Hille et al., 2018). While a myriad of structures have been determined for most types of CRISPR RNA-guided complexes (types I (Chowdhury et al., 2017; Jackson et al., 2014; Mulepati et al., 2014; Rollins et al., 2019; Xiao et al., 2018), II (Jiang et al., 2016; Jinek et al., 2014; Zhu et al., 2019), III (Jia et al., 2019; Sofos et al., 2020; Taylor et al., 2015; You et al., 2019), V (Li et al., 2021; Liu et al., 2019; Stella et al., 2017; Takeda et al., 2021; Zhang et al., 2020), and VI (Meeske et al., 2020; Slaymaker et al., 2019; Yan et al., 2018)), the RNP complexes of the highly diverse type IV CRISPR systems have largely remained structurally uncharacterized (Crowley et al., 2019; Faure et al., 2019; Makarova et al., 2020; Özcan et al., 2019; Taylor et al., 2019).

Type IV CRISPR systems primarily occur within plasmid-like elements, lack genes encoding adaptation modules (*cas1*, *cas2*, and *cas4*), and are classified into three distinct subtypes (IV-A, IV-B, IV-C) (Makarova et al., 2020; Özcan et al., 2019; Pinilla-Redondo et al., 2019). All type IV systems contain genes that encode for Csf2 (Cas7), Csf3 (Cas5), and Csf1 (large subunit) proteins, which assemble around an RNA to form a multi-subunit complex (Makarova et al., 2020; Özcan et al., 2019; Pinilla-Redondo et al., 2019). However, subtype-specific signature genes suggest distinct subtype functions. Type IV-A systems encode a DinG helicase shown to be essential for type IV-A mediated plasmid clearance (Crowley et al., 2019), Type IV-B systems contain the ancillary gene *cysH* of the phosphoadenosine phosphosulfate reductase family, and type IV-C systems encode a large subunit that contains an HD-nuclease domain (Makarova et al., 2020; Özcan et al., 2019; Pinilla-Redondo et al., 2019) (Figure S1). Additionally, type IV-A systems encode a CRISPR array and crRNA endonuclease, while type IV-B and type IV-C systems generally do not. It has been proposed that systems lacking a CRISPR array form complexes on crRNAs generated from other CRISPR systems (e.g. type I or type III), but this hypothesis has yet to be explored experimentally. Interestingly, the two subtypes that do not contain a CRISPR array (type IV-B and type IV-C) encode a small α -helical protein (Cas11) predicted to form part of the multi-subunit complex. Thus, there are two distinct type IV multi-subunit complexes, one that contains the small Cas11 subunit (types IV-B and IV-C), and another (type IV-A) that does not contain Cas11 but contains a crRNA derived from a type IV-A CRISPR array and processed by a type IV Cas6 endonuclease. To better understand the function of type IV CRISPR systems

¹Department of Molecular Biosciences, University of Texas at Austin, Austin, TX, USA

²Department of Chemistry and Biochemistry, Utah State University, Logan, UT, USA

³Laboratory of Microbiology, Wageningen University and Research, The Netherlands

⁴Institute for Cell and Molecular Biology, University of Texas at Austin, Austin, TX, USA

⁵Center for Systems and Synthetic Biology, University of Texas at Austin, Austin, TX, USA

⁶LIVESTRONG Cancer Institutes, Dell Medical School, Austin, TX, USA

⁷These authors contributed equally

⁸Lead contact

*Correspondence:

ryan.jackson@usu.edu

(R.N.J.),

raymond.staals@wur.nl

(R.H.J.S.),

dtaylor@utexas.edu (D.W.T.)

<https://doi.org/10.1016/j.isci.2021.102201>



as well as their subtype-specific similarities and differences, we isolated a type IV-B complex, analyzed the sequence of the small RNAs bound within the complex, and determined a near-atomic resolution structure.

RESULTS

The type IV-B RNP assembles on non-specific RNAs

The *Mycobacterium sp.* JS623 type IV-B CRISPR operon is encoded within a megaplasmid and lacks both a pre-crRNA maturase (Cas6/Csf5 (Özcan et al., 2019; Taylor et al., 2019)) and a CRISPR array, containing only *csf1* (Cas8-like large subunit), *cas11* (small subunit), *csf2* (Cas7) and *csf3* (Cas5) genes (Figure 1A). Interestingly, *M. sp.* JS623 also harbors a type I-E system (with an associated CRISPR array) on the same megaplasmid, and another type IV-B operon encoded on a different megaplasmid (Figure 1A), suggesting that type IV-B complexes may assemble on crRNAs encoded and processed by other CRISPR systems. However, the structure and function of such hybrid complexes are unknown.

To gain mechanistic insights into the type IV-B system, we transformed *E. coli* BL21 cells with an expression plasmid encoding the *M. sp.* JS623 type IV-B Cas proteins, and the *M. sp.* JS623 type I-E Cas6 and associated CRISPR array (Figure S2A). Using strep-tag affinity, size exclusion chromatography, and subsequent negative stain we observed filamentous RNP complexes that eluted close to the void volume and a smaller, discrete, RNA-containing species reminiscent of class 1 multi-subunit crRNA-guided complexes (Figure S2) (Makarova et al., 2017). While this latter fraction contained all four Csf subunits, Csf2 and Cas11 were the most abundant (Figure S2). Despite the appearance of a uniform band length of ~55–60 nucleotides on denaturing PAGE (Figures S2D and S3A), RNAseq analysis revealed bound RNAs were heterogeneous in sequence identity. Few RNAs were derived from the plasmid-encoded CRISPR array, while the majority of Csf-bound RNAs originated from the expression plasmid (63%) (Figures S3B and S3C). To exclude the possibility that this was due to low expression of the CRISPR array and/or lack of crRNA processing by Cas6, we repeated this analysis and compared it to an RNA-seq analysis of the total cellular population of RNAs (total RNA) extracted from the same host (Figure S3D). These results showed that the CRISPR array was indeed expressed and processed by Cas6, resulting in mature crRNAs with a typical eight nucleotide 5' handle (a characteristic for Cas6-mediated cleavages in the repeats). However, the mature crRNAs were not enriched in the RNAs isolated from type IV RNPs and were in low abundance (~0.12% of all reads). The apparent lack of sequence specific assembly of the Csf complex on mostly non-crRNAs is different from other CRISPR-Cas systems (Makarova et al., 2017), and might be indicative of a role of type IV CRISPR-Cas systems in functions other than antiviral defense.

The architecture of the type IV-B RNP resembles type III effector complexes

To compare the type IV-B RNP complex to the complexes of other class 1 systems, we next determined a cryo-EM structure of the IV-B Csf complex at 3.9 Å resolution (Figures 1B and S4, Table S1), allowing us to build an atomic model of the complex *de novo* (Figure 1C). The type IV-B complex resembles a sea cucumber, with six Csf2 (Cas7-like) subunits forming a helical “backbone,” and five Cas11 subunits comprising a helical “belly”. Each Cas11 subunit sits upon a Csf2-Csf2 interface (Figures 1D–1F). The “ α -helix bundle” topology of Cas11 (Figure S5C) and presence of a contiguous positively-charged patch running along the length of the minor filament (Figure S6) are typical of Cas11 small subunits in class 1 CRISPR systems (Rollins et al., 2019; Xiao et al., 2017), although the arrangement of helices within type IV Cas11 is distinct from type I and type III small subunits.

Like other class 1 Cas7 proteins, Csf2 adopts a hand-shaped structure with fingers, a palm, and a thumb. The palm makes extensive contacts with the bound RNA (buried surface area of ~1200 Å² per Csf2 subunit) (Figure 2A), while the thumbs of neighboring Csf2 subunits protrude into the center of the palm, inducing a kink in the RNA backbone and a “flipped” base at six nucleotide intervals (typical of other class 1 complexes (Jackson et al., 2014; Taylor et al., 2015)). Using our atomic model of Csf2, we searched for structural homologs. Csf2 had significant similarity to the type III-A CRISPR Csm3 (i.e. Cas7) subunit (Dali Z score of 14.1), despite a sequence identity of only 16%. Csf2 and Csm3 superimpose with an r.m.s.d of 2.9 Å and use equivalent interfaces to bind RNA and induce near-identical RNA backbone conformations (r.m.s.d of 1.5 Å) (Figure 2A). This supports previous bioinformatics-based hypotheses that type IV systems originated from type III-like ancestors (Makarova et al., 2020; Özcan et al., 2019; Pinilla-Redondo et al., 2019).

The type III backbone protein Csm3 cleaves the phosphodiester backbone of crRNA-bound target strand (TS) RNA at 6-nt intervals (Staals et al., 2014; Steens et al., 2021). Given that the Csm crRNA aligns almost

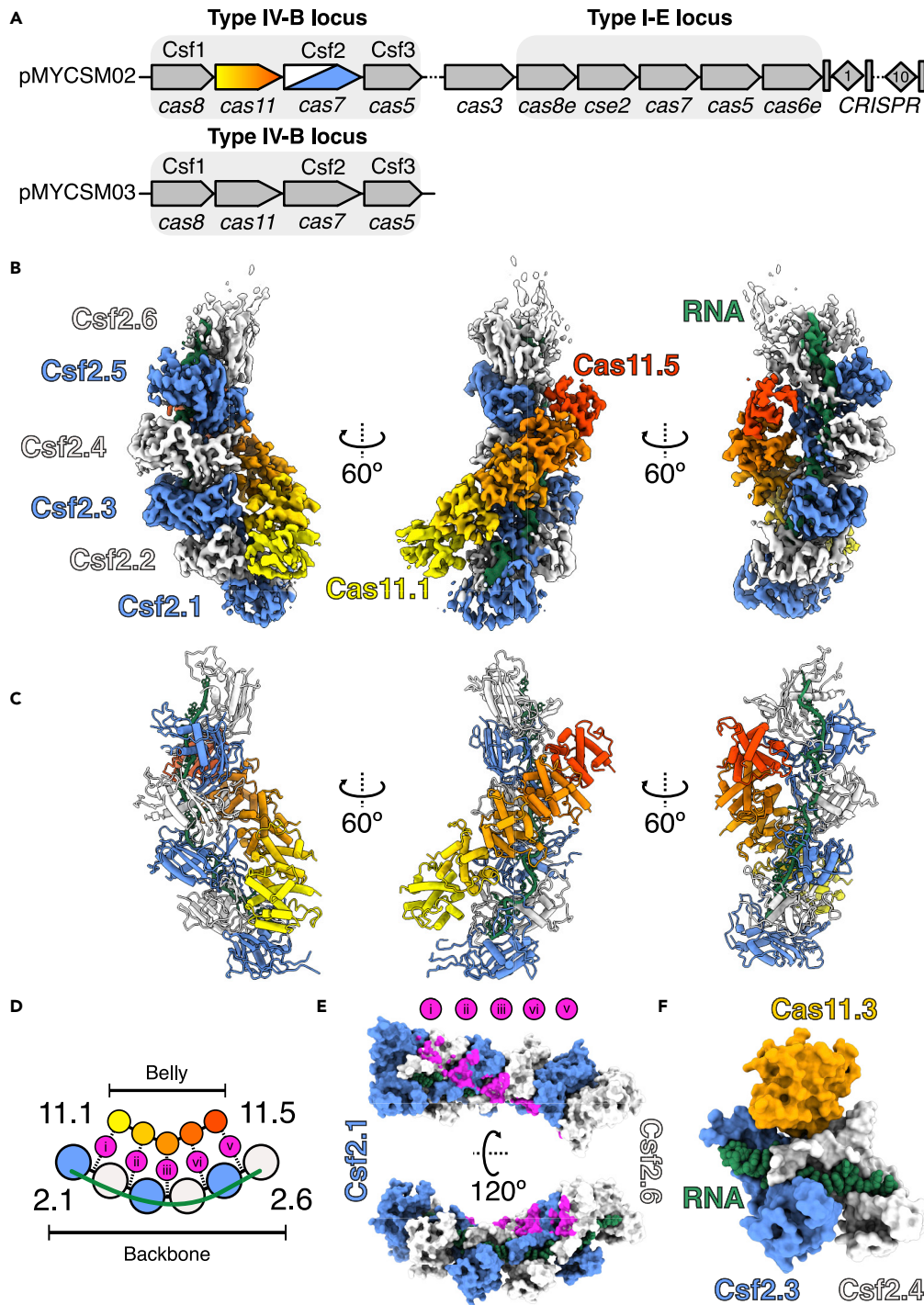


Figure 1. Structure of type IV-B CRISPR complex

See also [Figures S1–S4](#) and [Table S1](#).

(A) *M. sp.* JS623 plasmid-encoded CRISPR operons. Top: Type IV-B and I-E CRISPR loci present on pMYCSM02 megaplasmid. Bottom: Additional type IV-B locus encoded by pMYCSM03 megaplasmid. Genes predicted to encode RNP complex subunits are indicated with a gray rectangle.

(B) 3.9 Å-resolution cryo-EM reconstruction of type IV-B CRISPR complex. Cas7 subunits are colored blue and white, and five Cas11 subunits are colored as a yellow-orange-red gradient. Csf-bound RNA is green.

(C) Refined model for the Csf effector complex derived from the cryo-EM maps shown in (B).

Figure 1. Continued

(D) Schematic of Cas7-Cas11 interactions. Five Csf2-Cas11 interactions occur in this complex (labeled i – v).
 (E) Positions of Cas11 contacts on Csf2 backbone, colored magenta as shown in panel D. Cas11 sits upon the Csf2-Csf2 interface.
 (F) Cas11 binds at the interface with buried surface area of 505 Å² (150 Å² and 355 Å² with Csf2.3 and Csf2.4, respectively). Cas11 is completely occluded from bound RNA. Csf2 subunits are intimately connected (1021 Å²) and make a network of contacts with bound RNA (~1200 Å² buried surface area per Csf2 subunit).

perfectly with Csf-bound RNA, we reasoned that Csf2 might also possess RNase activity. Within our aligned structures, both the catalytic Asp36^{Csm3} residue and the conserved Asp42^{Csf2} residue are similarly positioned within an unstructured “catalytic loop” (Figures 2C–2E and S7). However, despite this similarity, structural alignment with a target-bound type III complex reveals significant steric clashes between the path of the bound nucleic acid target and the Csf2 catalytic loop (Figures 2F and 2G), suggesting a significant conformational rearrangement of subunits would need to occur upon target binding to place = Asp42^{Csf2} in a position amenable to catalyze target RNA cleavage. Thus, additional substrate bound structures and *in vitro* functional assays are needed to more fully explore the possibility of Csf2-mediated RNase activity.

DISCUSSION

Our structure of the Csf complex provides evidence that type IV-B evolved from type III CRISPR-Cas systems but lost its CRISPR and Cas6-based crRNA processing activity due to functional respecialization. Although the *M. sp.* JS623 type IV-B operon contains both Csf3 (Cas5) and the putative large subunit Csf1, we did not observe corresponding densities within the high-resolution cryo-EM structure. However, bands that correspond to Csf1 and Csf3 are observed in SDS-PAGE analysis of the sample (Figure S2D), and there is unmodeled ambiguous density on the top and bottom of the complex that could represent a flexible association with Csf1 and Csf3 or additional Csf2 subunits. In type I CRISPR systems, Cas5 binds the 5' crRNA handle with high affinity and sequence specificity, nucleating complex assembly (Chowdhury et al., 2017; Hochstrasser et al., 2016; Jia et al., 2019). The lack of discernible density for the Cas5-like Csf3 subunit within our complex may explain the heterogeneous assembly of type IV-B Csf complexes around non-specific RNA (Figure S3). However, because the type IV-B system does not encode a CRISPR array, the identity of the RNA sequence that Csf3 would specifically recognize is unknown. Indeed, it remains to be determined whether Csf3 truly serves a similar role to the Cas5 subunits in other systems, binding the 5'-handle of processed crRNAs. We hypothesized that crRNAs generated from the adjacent type I-E CRISPR and Cas6 endonuclease would be bound by the type IV-B complex. However, our sequencing analysis showed no enrichment for crRNAs within the RNPs or any other RNAs available in the total sample. Interestingly, recent bioinformatic analysis indicated a negative co-occurrence of type IV-B systems with other CRISPR systems suggesting their function is not dependent on co-occurring CRISPR arrays (Pinilla-Redondo et al., 2019). The ability of the Csf complex to assemble on non-specific RNAs of a uniform length suggests that type IV-B systems may have been functionally repurposed for a yet to be identified role.

The lack of discernible density for the Csf3 and Csf1 subunits suggests our structure may not accurately reflect the functional type IV-B Csf effector complex. However, several lines of reasoning argue that even without obvious density for Csf1 and Csf3, this complex provides important insights into understanding type IV-B system function. Superposition of the helical Cas7 backbones from type III effector complexes with our structure shows that they are nearly identical in arrangement (Figure S5A). Additionally, the crRNA from the type IV RNP can be overlaid on that of the type III effector with an r.m.s.d. of 1.5 Å (Figure 2A), indicating our complex presents RNA in a conformation amenable for base pairing with complementary nucleic acid. In fact, studies have shown that there are no structural differences between filaments assembled around non-specific RNAs and correctly processed crRNAs bound to the effector (Hochstrasser et al., 2016). Importantly, the structures of all CRISPR-Cas effector complexes involve non-sequence specific interactions between the crRNA and Cas7-like backbone proteins, suggesting that there would be no structural differences between a random RNA and a crRNA bound within the Cas7 backbone of an RNP complex. Thus, our structure likely accurately represents the structure of the Cas7-like core of the effector complex even though it is bound to heterogeneous RNA, and no density is observed for Csf1 and Csf3. Completely novel information is gleaned from our cryo-EM reconstruction of the type IV-B RNP including (1) the first structure of a type IV Cas11 protein, which adopts a novel small subunit fold, (2) the first structure of a Cas7-like Csf2 subunit, and (3) interactions between these subunits with each other and with bound RNA.

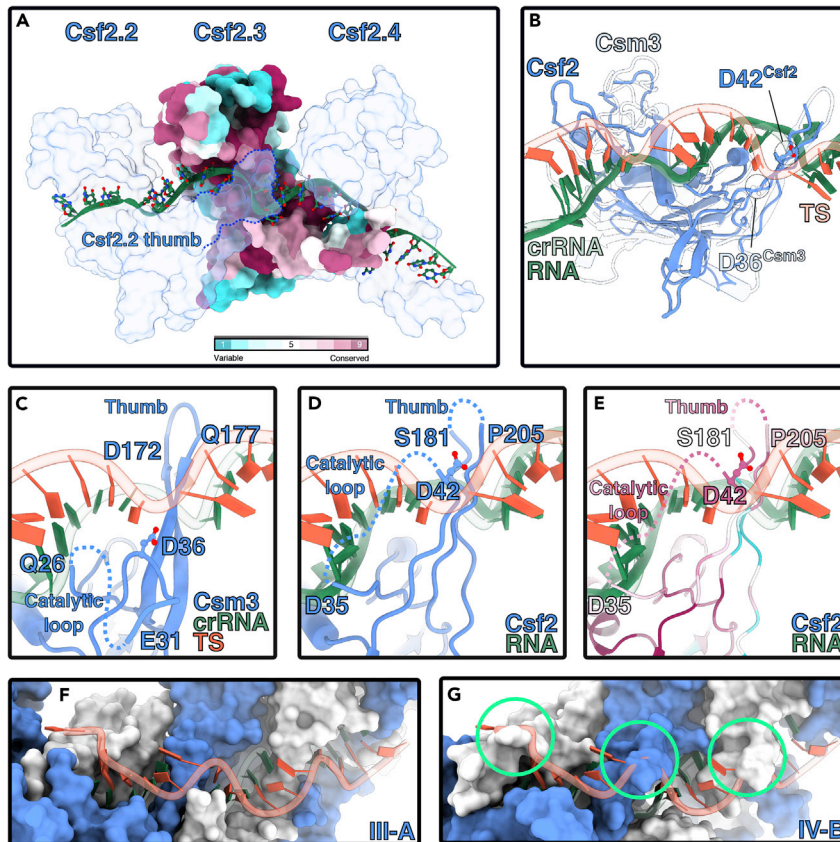


Figure 2. RNA-binding by type IV-B Cas7

See also [Figures S5–S7](#).

- (A) RNA (green) binding site runs across the palms of Csf2 subunits. Csf2.3 is colored according to conservation. The “thumb” of the n_{-1} Csf2 (i.e. Csf2.2) protrudes into the backbone of bound RNA (solid green), inducing a kink.
- (B) Alignment of type III-A backbone subunit Csm3 (PDB 607i, transparent) with Csf2 (solid blue). Csm3 and Csf2 align with an r.m.s.d. of 2.9Å, with a Dali server Dali server Z score 14.1. Csf2-bound RNA binds in the same conformation as crRNA (transparent green) to Csm3 (RMSD of 1.5 Å). Catalytic residue Asp36^{Csm3} and putative catalytic residue Asp42^{Csf2} side chains are located near the target strand (TS - transparent red), bound to the type III crRNA (transparent green).
- (C) Residues flanking unstructured catalytic loop (27–35) and apical loop of Csm3 thumb also interact with the TS. Catalytic residue D36 is shown for clarity.
- (D) Putative interactions with Csf2 and TS, based on alignments with the Csm complex.
- (E) Putative interactions colored by conservation. The Csf2 thumb contains a flexible 20 residue insertion, not visible in our cryo-EM map.
- (F), Path of TS bound by type III-A Csm complex.
- (G) Putative path of TS along IV-B. Severe classes with TS and Csf2 are circled in green.

Since all type IV systems identified lack adaptation subunits and almost all (97.8%) type IV-B operons identified lack a CRISPR array, it is likely they do not participate in selective pre-spacer acquisition or adaptive immunity ([Makarova et al., 2020](#); [Özcan et al., 2019](#); [Pinilla-Redondo et al., 2019](#)). Instead, they may have been co-opted for an orthogonal function. While there is a precedent for the repurposing of CRISPR systems for non-defense functions ([Halpin-Healy et al., 2020](#); [Klomp et al., 2019](#)), the role of type IV-B systems remains a mystery. A particularly tantalizing hypothesis is that type IV-B Csf complexes assemble on small RNAs, acting as non-specific RNA-sponges, and enabling IV-B-encoding megaplasmids to evade targeting by host cell RNA guided defenses ([Pinilla-Redondo et al., 2019](#)). Future experiments are essential to reveal the biological functions of type IV systems. Recent classifications have indicated that although type IV-B systems are highly diverse, they are almost always associated with an adenosine 5'-phosphosulfate reductase-family gene *cysH* ([Makarova et al., 2020](#); [Özcan et al., 2019](#); [Pinilla-Redondo et al., 2019](#)) ([Figure S1](#)). Thus, understanding the interplay between *cysH* and the type IV-B Csf RNP complex may be the key to deciphering the enigmatic role of type IV-B CRISPR systems.

Limitations of the study

The current structure lacks discernible density for Csf1 and Csf3 proteins. The equivalent subunits in Type I systems are responsible for specific functions. Without complementary functional *in vitro* and *in vivo* data, it is impossible to unambiguously characterize the current structure as a functional effector complex.

Resource availability

Lead contact

Further information and requests for resources and reagents should be directed to and will be fulfilled by the lead contact, David W. Taylor (dtaylor@utexas.edu).

Materials availability

All unique/stable reagents generated in this study are available from the lead contact without restriction.

Data and code availability

The cryo-EM structure and associated atomic coordinates have been deposited in the Electron Microscopy DataBank and the Protein DataBank with accession codes EMD-22340 and PDB: 7JHY, respectively. The accession number for the RNA sequencing data reported in this paper is SRA: SUB8825456.

METHODS

All methods can be found in the accompanying [Transparent methods supplemental file](#).

SUPPLEMENTAL INFORMATION

Supplemental information can be found online at <https://doi.org/10.1016/j.isci.2021.102201>.

ACKNOWLEDGMENTS

We thank members of the Staals, Jackson, and Taylor labs for helpful discussions. This work was supported in part by Welch Foundation grant F-1938 (to D.W.T.), Army Research Office Grant W911NF-15-1-0120 (to D.W.T.), National Institute of General Medical Sciences (NIGMS) of the National Institutes of Health (NIH) R35GM138348 (to D.W.T.), and a Robert J. Kleberg, Jr. and Helen C. Kleberg Foundation Medical Research Award (to D.W.T.). D.W.T. is a CPRIT Scholar supported by the Cancer Prevention and Research Institute of Texas (RR160088) and an Army Young Investigator supported by the Army Research Office (W911NF-19-1-0021). This work was also supported by the David Taylor Excellence Fund in Structural Biology made possible with support from Judy and Henry Sauer (to D.W.T.). Research in the Jackson Lab is supported by Utah State University New Faculty Start-up funding from the Department of Chemistry and Biochemistry, the Research and Graduate Studies Office, and the College of Science as well as the National Institute of General Medical Sciences (NIGMS) of the National Institutes of Health (NIH) R35GM138080. R.H.J.S. is supported by a VENI grant (016.Veni.171.047) from The Netherlands Organization for Scientific Research (NWO). Data were collected at the Sauer Structural Biology Lab at the University of Texas at Austin.

AUTHORS CONTRIBUTION

H.N.T. and J.A.S. performed purification of complexes. Y.Z. and J.P.K.B. collected and processed cryo-EM data. Y.Z., H.N.T., R.N.J. and J.P.K.B. performed the model-building and Y.Z. and J.P.K.B. performed model refinement. J.A.S. and H.N.T. performed the RNA-seq experiments. All authors interpreted the results and wrote the manuscript. R.H.J.S., R.N.J., and D.W.T. conceived the experiments, supervised the research, and secured funding for the project.

DECLARATION OF INTERESTS

The authors declare no competing interests.

Received: July 21, 2020

Revised: January 3, 2021

Accepted: February 12, 2021

Published: March 19, 2021

REFERENCES

- Chowdhury, S., Carter, J., Rollins, M.C.F., Golden, S.M., Jackson, R.N., Hoffmann, C., Nosaka, L., Bondy-Denomy, J., Maxwell, K.L., Davidson, A.R., et al. (2017). Structure reveals mechanisms of viral suppressors that intercept a CRISPR RNA-guided surveillance complex. *Cell* 169, 47–57.e11.
- Crowley, V.M., Catching, A., Taylor, H.N., Borges, A.L., Metcalf, J., Bondy-Denomy, J., and Jackson, R.N. (2019). A type IV-A CRISPR-cas system in *Pseudomonas aeruginosa* mediates RNA-guided plasmid interference in vivo. *Cris. J.* 2, 434–440.
- Faure, G., Shmakov, S.A., Yan, W.X., Cheng, D.R., Scott, D.A., Peters, J.E., Makarova, K.S., and Koonin, E.V. (2019). CRISPR–Cas in mobile genetic elements: counter-defence and beyond. *Nat. Rev. Microbiol.* 17, 513–525.
- Halpin-Healy, T.S., Klompe, S.E., Sternberg, S.H., and Fernández, I.S. (2020). Structural basis of DNA targeting by a transposon-encoded CRISPR–Cas system. *Nature* 577, 271–274.
- Hille, F., Richter, H., Wong, S.P., Bratovič, M., Ressel, S., and Charpentier, E. (2018). The biology of CRISPR-cas: backward and forward. *Cell* 172, 1239–1259.
- Hochstrasser, M.L., Taylor, D.W., Kornfeld, J.E., Nogales, E., and Doudna, J.A. (2016). DNA targeting by a minimal CRISPR RNA-guided cascade. *Mol. Cell* 63, 840–851.
- Jackson, R.N., Golden, S.M., van Erp, P.B.G., Carter, J., Westra, E.R., Brouns, S.J.J., van der Oost, J., Terwilliger, T.C., Read, R.J., and Wiedenheft, B. (2014). Structural biology. Crystal structure of the CRISPR RNA-guided surveillance complex from *Escherichia coli*. *Science* 345, 1473–1479.
- Jia, N., Mo, C.Y., Wang, C., Eng, E.T., Marraffini, L.A., and Patel, D.J. (2019). Type III-A CRISPR-cas Csm complexes: assembly, periodic RNA cleavage, DNase activity regulation, and autoimmunity. *Mol. Cell* 73, 264–277.e5.
- Jiang, F., Taylor, D.W., Chen, J.S., Kornfeld, J.E., Zhou, K., Thompson, A.J., Nogales, E., and Doudna, J.A. (2016). Structures of a CRISPR–Cas9 R-loop complex primed for DNA cleavage. *Science* 351, 867–871.
- Jinek, M., Jiang, F., Taylor, D.W., Sternberg, S.H., Kaya, E., Ma, E., Anders, C., Hauer, M., Zhou, K., Lin, S., et al. (2014). Structures of Cas9 endonucleases reveal RNA-mediated conformational activation. *Science* 343, 1247997.
- Klompe, S.E., Vo, P.L.H., Halpin-Healy, T.S., and Sternberg, S.H. (2019). Transposon-encoded CRISPR–Cas systems direct RNA-guided DNA integration. *Nature* 571, 219–225.
- Li, Z., Zhang, H., Xiao, R., Han, R., and Chang, L. (2021). Cryo-EM structure of the RNA-guided ribonuclease Cas12g. *Nat. Chem. Biol.* <https://doi.org/10.1038/s41589-020-00721-2>.
- Liu, J.J., Orlova, N., Oakes, B.L., Ma, E., Spinner, H.B., Baney, K.L.M., Chuck, J., Tan, D., Knott, G.J., Harrington, L.B., et al. (2019). CasX enzymes comprise a distinct family of RNA-guided genome editors. *Nature* 566, 218–223.
- Makarova, K.S., Wolf, Y.I., Iranzo, J., Shmakov, S.A., Alkhnbashi, O.S., Brouns, S.J.J., Charpentier, E., Cheng, D., Haft, D.H., Horvath, P., et al. (2020). Evolutionary classification of CRISPR–Cas systems: a burst of class 2 and derived variants. *Nat. Rev. Microbiol.* 18, 67–83.
- Makarova, K.S., Zhang, F., and Koonin, E.V. (2017). SnapShot: class 1 CRISPR-cas systems. *Cell* 168, 946–946.e1.
- Meeske, A.J., Jia, N., Cassel, A.K., Kozlova, A., Liao, J., Wiedmann, M., Patel, D.J., and Marraffini, L.A. (2020). A phage-encoded anti-CRISPR enables complete evasion of type VI-A CRISPR–Cas immunity. *Science* 369, 54–59.
- Mulepati, S., Héroux, A., and Bailey, S. (2014). Crystal structure of a CRISPR RNA-guided surveillance complex bound to a ssDNA target. *Science* 345, 1479–1484.
- Özcan, A., Pausch, P., Linden, A., Wulf, A., Schühle, K., Heider, J., Urlaub, H., Heimerl, T., Bange, G., and Randau, L. (2019). Type IV CRISPR RNA processing and effector complex formation in *Aromatoleum aromaticum*. *Nat. Microbiol.* 4, 89–96.
- Pinilla-Redondo, R., Mayo-Muñoz, D., Russel, J., Garrett, R.A., Randau, L., Sørensen, S.J., and Shah, S.A. (2019). Type IV CRISPR–Cas systems are highly diverse and involved in competition between plasmids. *Nucleic Acids Res.* 48, 2000–2012.
- Rollins, M.C.F., Chowdhury, S., Carter, J., Golden, S.M., Miettinen, H.M., Santiago-Frangos, A., Faith, D., Lawrence, C.M., Lander, G.C., and Wiedenheft, B. (2019). Structure reveals a mechanism of CRISPR-RNA-guided nuclease recruitment and anti-CRISPR viral mimicry. *Mol. Cell* 74, 132–142.e5.
- Slaymaker, I.M., Mesa, P., Kellner, M.J., Kannan, S., Brignole, E., Koob, J., Feliciano, P.R., Stella, S., Abudayyeh, O.O., Gootenberg, J.S., et al. (2019). High-resolution structure of Cas13b and biochemical characterization of RNA targeting and cleavage. *Cell Rep.* 26, 3741–3751.e5.
- Sofos, N., Feng, M., Stella, S., Pape, T., Fuglsang, A., Lin, J., Huang, Q., Li, Y., She, Q., and Montoya, G. (2020). Structures of the *cmr-β* complex reveal the regulation of the immunity mechanism of type III-B CRISPR-cas. *Mol. Cell* 79, 741–757.e7.
- Staals, R.H.J., Zhu, Y., Taylor, D.W., Kornfeld, J.E., Sharma, K., Barendregt, A., Koehorst, J.J., Vlot, M., Neupane, N., Varossieau, K., et al. (2014). RNA targeting by the type III-A CRISPR-cas Csm complex of *thermus thermophilus*. *Mol. Cell* 56, 518–530.
- Steens, J.A., Zhu, Y., Taylor, D.W., Bravo, J.P.K., Prinsen, S.H.P., Schoen, C.D., Keijser, B.J.F., Ossendrijver, M., Hofstra, L.M., Brouns, S.J.J., et al. (2021). SCOPE: Flexible Targeting and Stringent CARF Activation Enables Type III CRISPR–Cas Diagnostics. *bioRxiv*. <https://doi.org/10.1101/2021.02.01.429135>.
- Stella, S., Alcón, P., and Montoya, G. (2017). Structure of the Cpf1 endonuclease R-loop complex after target DNA cleavage. *Nature* 546, 559–563.
- Takeda, S.N., Nakagawa, R., Okazaki, S., Hirano, H., Kobayashi, K., Kusakizako, T., Nishizawa, T., Yamashita, K., Nishimasu, H., and Nureki, O. (2021). Structure of the miniature type V-F CRISPR–Cas effector enzyme. *Mol. Cell* 81, 558–570.e3.
- Taylor, D.W., Zhu, Y., Staals, R.H.J., Kornfeld, J.E., Shinkai, A., Oost, J., Nogales, E., and Doudna, J.A. (2015). Structure of the CRISPR–Cmr complex reveal mode of RNA target positioning. *Science* 348, 581–586.
- Taylor, H.N., Warner, E.E., Armbrust, M.J., Crowley, V.M., Olsen, K.J., and Jackson, R.N. (2019). Structural basis of Type IV CRISPR RNA biogenesis by a Cas6 endoribonuclease. *RNA Biol.* 16, 1438–1447.
- Xiao, Y., Luo, M., Hayes, R.P., Kim, J., Ng, S., Ding, F., Liao, M., and Ke, A. (2017). Structure basis for directional R-loop formation and substrate handover mechanisms in type I CRISPR-cas system. *Cell* 170, 48–60.e11.
- Xiao, Y., Xiao, Yibei, Luo, M., Dolan, A.E., Liao, M., and Ke, A. (2018). Structure basis for RNA-guided DNA degradation by cascade and Cas3. *Science* 361, eatt0839.
- Yan, W.X., Chong, S., Zhang, H., Makarova, K.S., Koonin, E.V., Cheng, D.R., and Scott, D.A. (2018). Cas13d is a compact RNA-targeting type VI CRISPR effector positively modulated by a WYL-domain-containing accessory protein. *Mol. Cell* 70, 327–339.e5.
- You, L., Ma, J., Wang, J., Artamonova, D., Wang, M., Liu, L., Xiang, H., Severinov, K., Zhang, X., and Wang, Y. (2019). Structure studies of the CRISPR-csm complex reveal mechanism of Co-transcriptional interference. *Cell* 176, 239–253.e16.
- Zhang, H., Li, Z., Xiao, R., and Chang, L. (2020). Mechanisms for target recognition and cleavage by the Cas12i RNA-guided endonuclease. *Nat. Struct. Mol. Biol.* 27, 1069–1076.
- Zhu, X., Clarke, R., Puppala, A.K., Chittori, S., Merk, A., Merrill, B.J., Simonović, M., and Subramaniam, S. (2019). Cryo-EM structures reveal coordinated domain motions that govern DNA cleavage by Cas9. *Nat. Struct. Mol. Biol.* 26, 679–685.

iScience, Volume 24

Supplemental information

Structure of a type IV CRISPR-Cas

ribonucleoprotein complex

Yi Zhou, Jack P.K. Bravo, Hannah N. Taylor, Jurre A. Steens, Ryan N. Jackson, Raymond H.J. Staals, and David W. Taylor

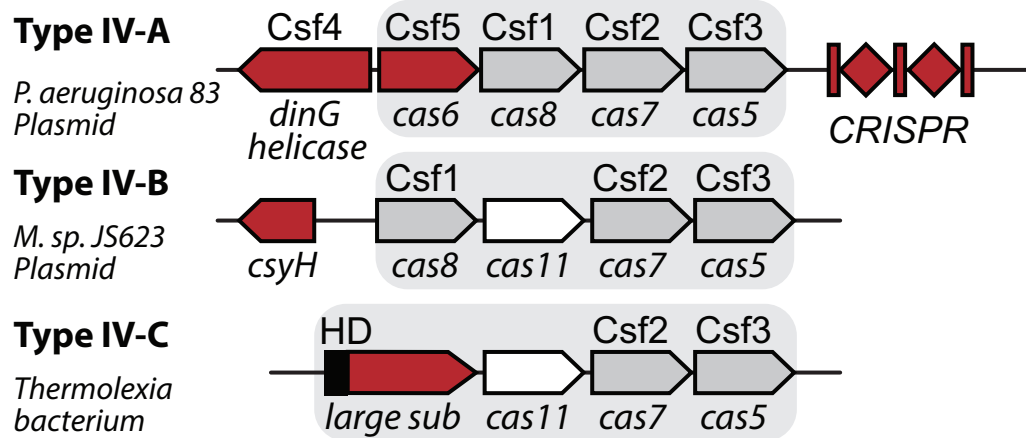


Figure S1. Classification of type IV subtypes. Related to Figure 1. Schematic of the three distinct type IV subtypes defined in (Makarova et al., 2020). Genetic features (genes and CRISPRs) found primarily in a single subtype are colored red. Gray rectangles indicate genes expected to encode proteins that form RNP complexes. The *cas11* gene is colored white to highlight that it is found within the subtypes lacking a CRISPR (subtypes IV-B and IV-C). The HD nuclease domain of the *cas8*-like subunit of IV-C is colored black.

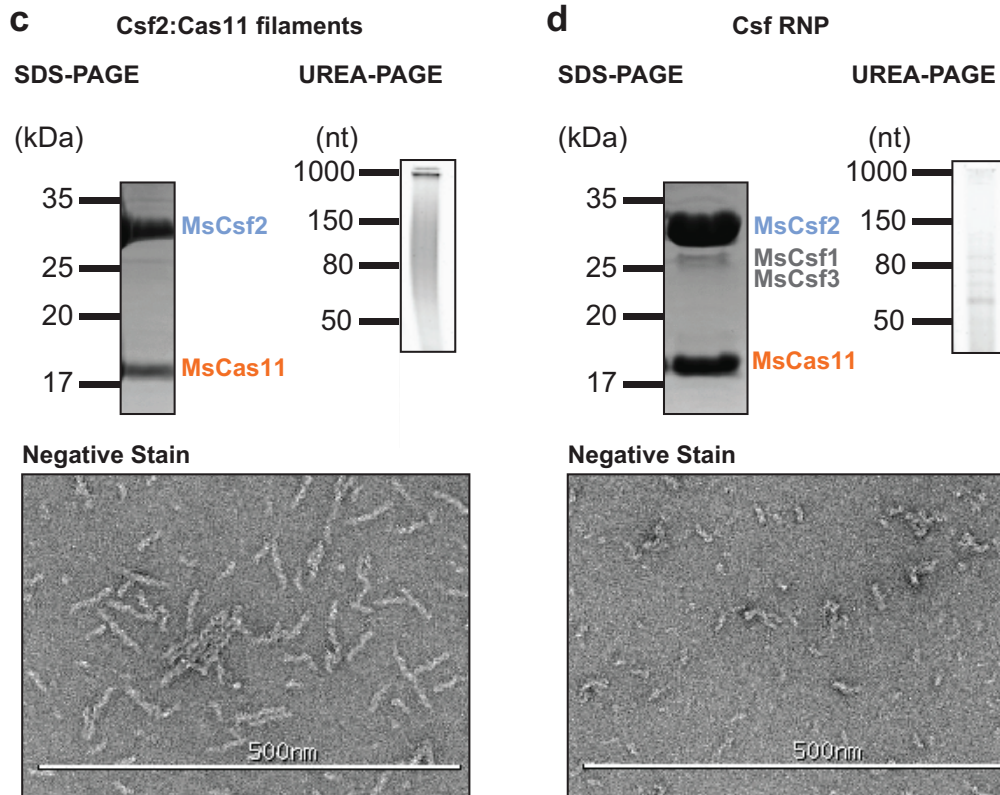
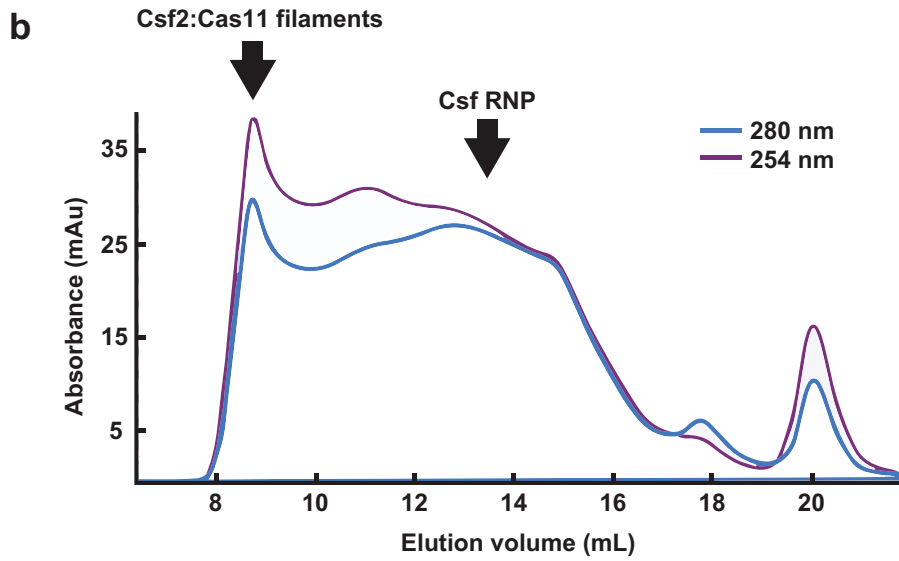
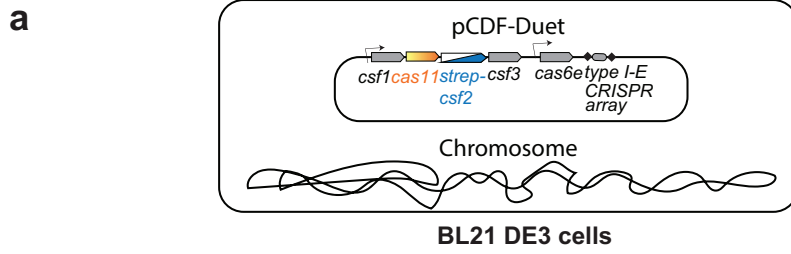


Figure S2. Purification of the *M. sp JS623* RNP complex by affinity chromatography (N-Strep-MsCsf2) and size exclusion chromatography. Related to Figure 1. a, Diagram of plasmid used to express the type IV-B complex in BL21 DE3 cells. b, SEC chromatogram highlighting peaks corresponding to Csf2:Cas11 filaments and the RNP complex. c, SDS-PAGE, UREA-PAGE, and negative stain data indicating the presence of Csf2:Cas11 bound to long RNAs to create filamentous structures. d, SDS-PAGE, UREA-PAGE, and negative stain data indicating the presence of Csf1, Csf2, Csf3, and Cas11 bound to short, distinct RNAs to create an RNP complex.

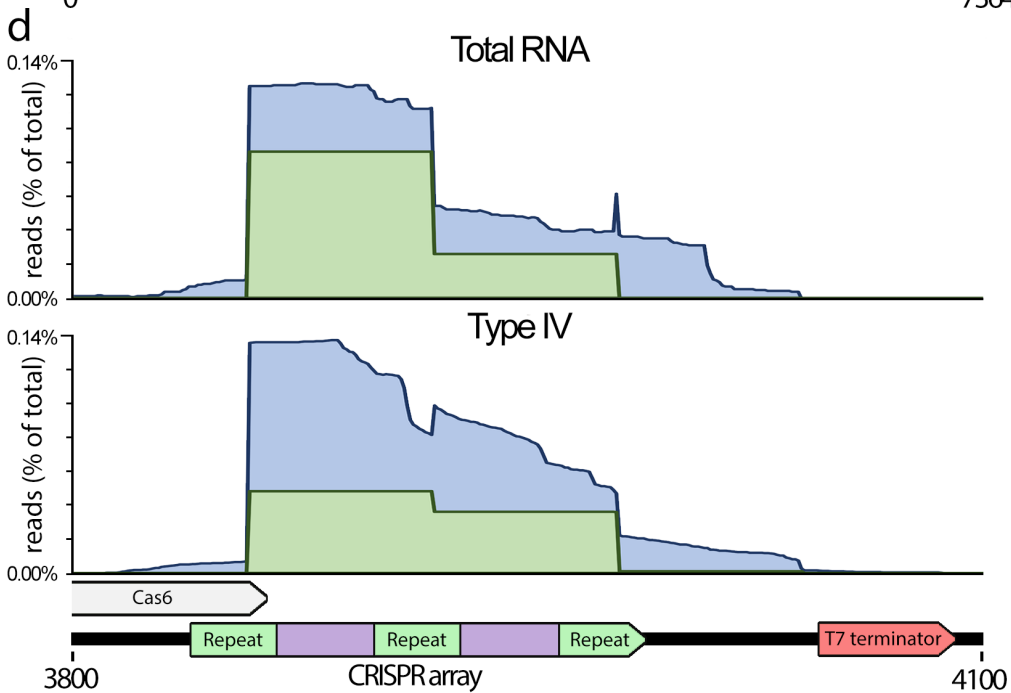
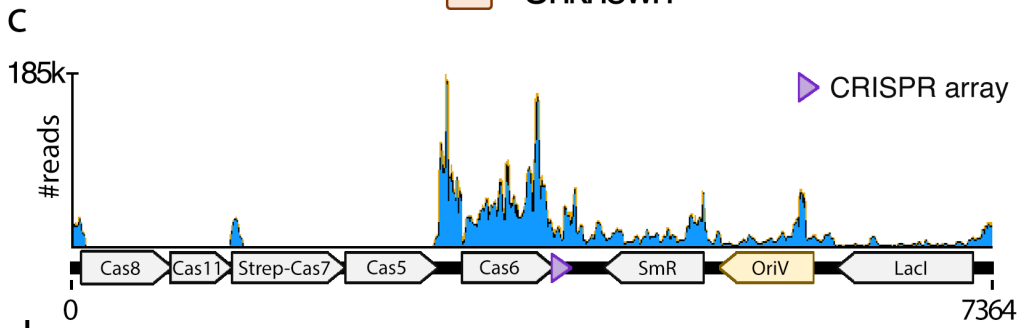
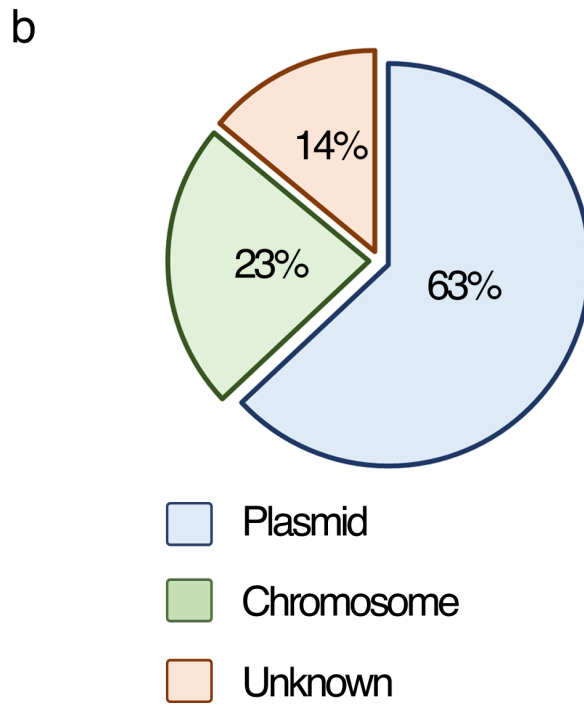
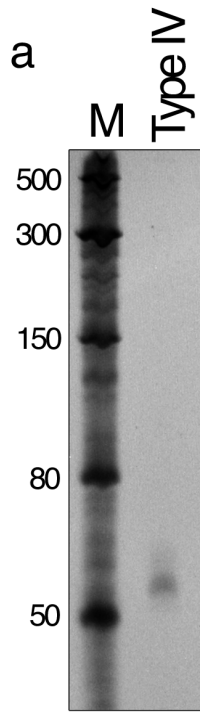


Figure S3. RNA sequencing on co-purifying nucleotides with type IV complex. Related to Figure 1. **a**, UREA-PAGE gel showing nucleic acids co-purifying with the type IV-B complex. The triangle indicates the ~60nt band purified from isolated type IV-B complexes that was used for RNA sequencing analysis. **b**, Percentage of reads mapping to either to expression plasmid, chromosome, or of unknown origin. **c**, Distribution of reads mapping on the expression plasmid. **d**, Comparison of repeat-containing RNAs from the total cellular RNA population (“total RNA”) and type IV RNP-associated (“type IV”) RNAs mapped on the CRISPR array of the expression plasmid (in blue). Reads indicated in green represent the 61-nt RNAs with a perfect repeat-derived 8-nt 5’ handle, reminiscent of Cas6-mediated cleavages in the repeats.

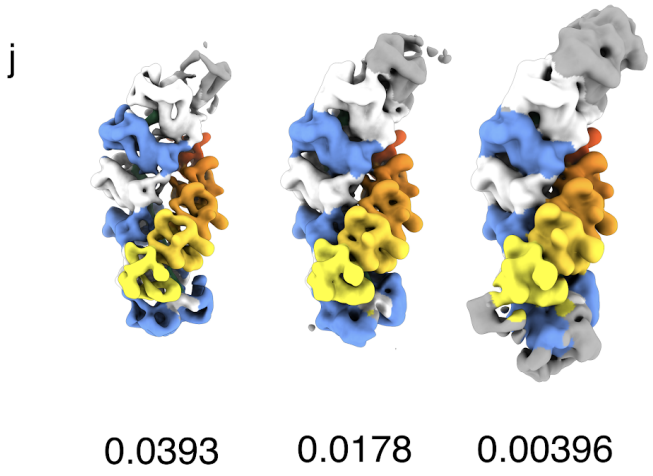
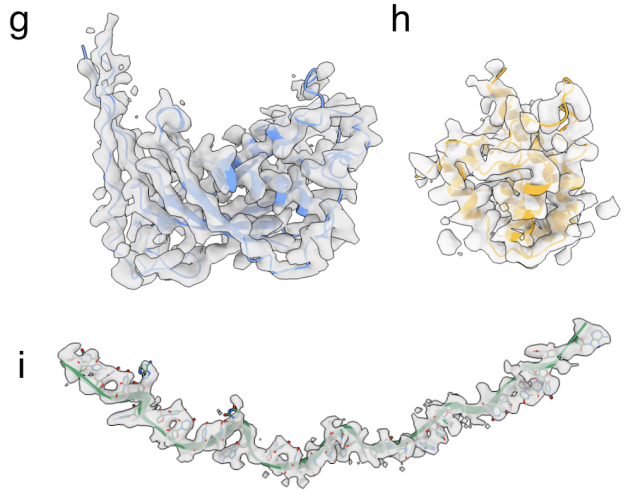
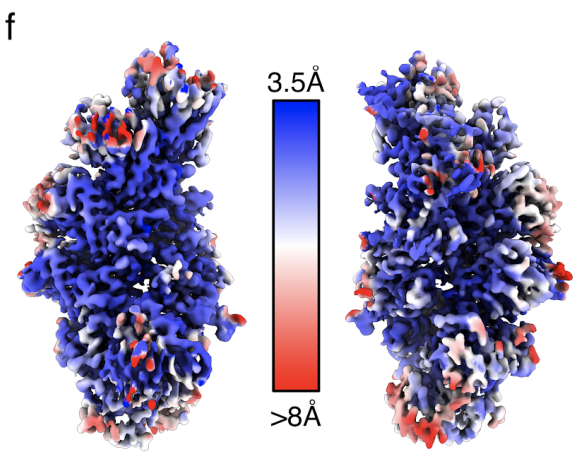
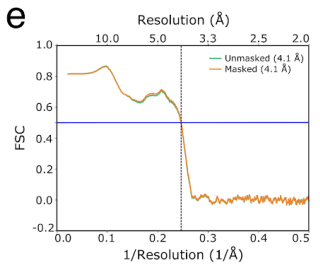
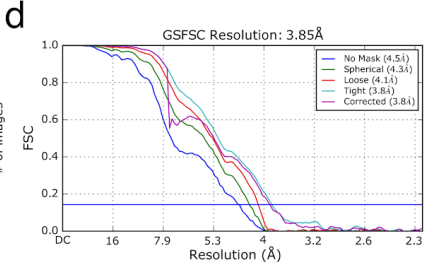
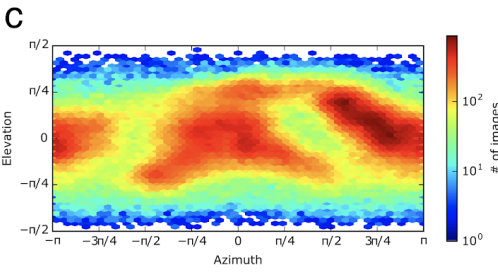
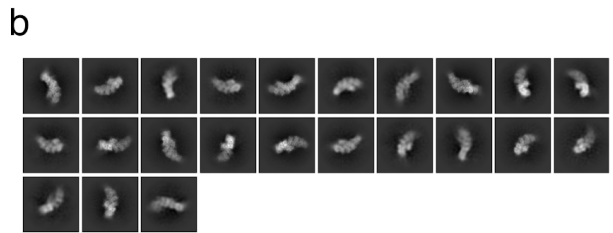
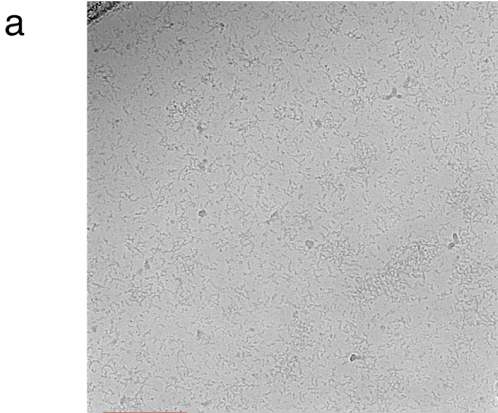


Figure S4. Cryo-EM analysis of Csf. Related to Figure 1. **a**, Representative micrograph of Csf complex particles. **b**, 2D class averages of discrete Csf oligomers used for 3D reconstruction. **c**, Euler angular distribution of particles contributing to final 3D reconstruction. **d**, Fourier shell correlation (FSC) of final 3D reconstruction, with a global resolution of 3.9 Å at the 0.143 threshold. **e**, Map-to-model FSC, with a model resolution of 4.1 Å at the 0.5 threshold. **f**, Map of Csf complex colored by local resolution. **g – i**, Representative atomic models and corresponding cryo-EM densities for Csf2 (**g**), Cas11 (**h**) and RNA (**i**). **j**, Low-pass filtered (8 Å) map of Csf complex at three different isosurface thresholds. At lower thresholds (0.0178 & 0.00396), additional density appears at the top of the complex. This density may correspond to Csf1 Csf3 subunits, however the low resolution of this region makes unambiguous subunit assignment impossible.

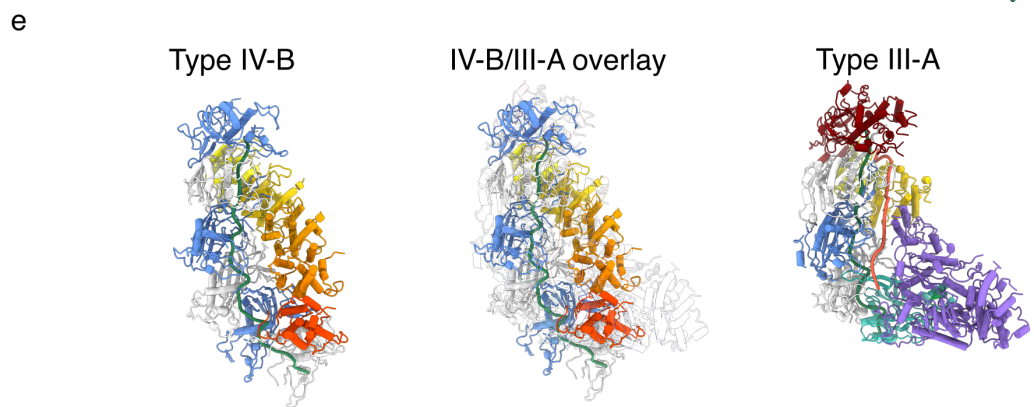
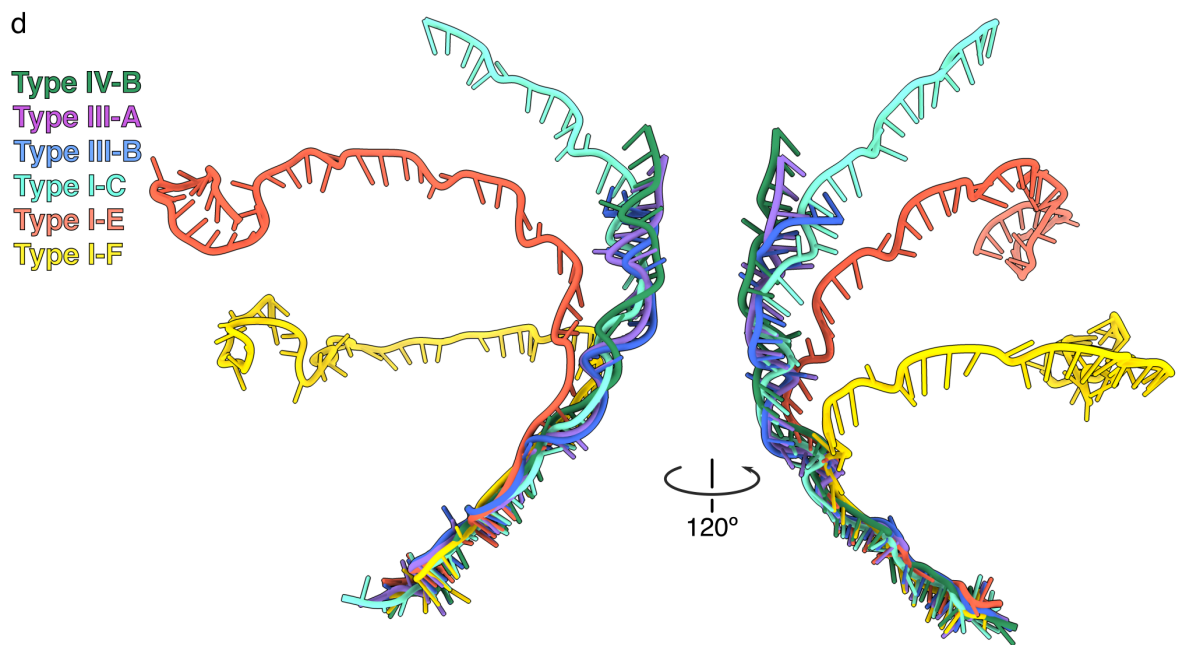
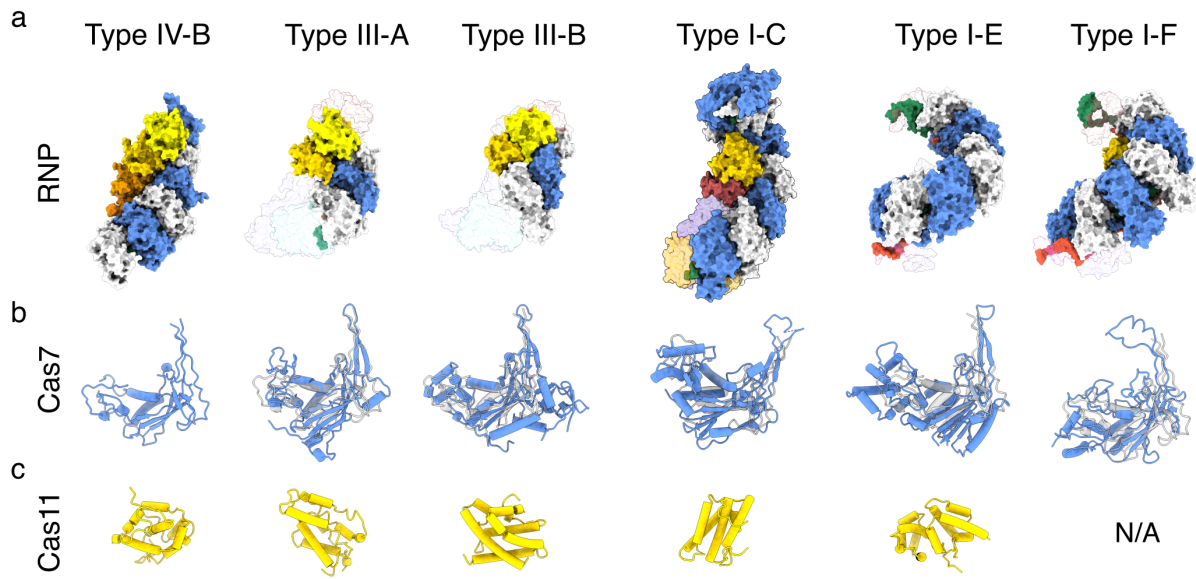


Figure S5. Comparison to Cascade complexes. Related to Figure 2. **a**, Comparison of Type IV-B Csf with other effector/Cascade complexes. crRNA within Type III-A (PDB 6o7i) (Jia et al., 2019), III-B (PDB 3x1l) (Osawa et al., 2015) & I-C (O'Brien et al., 2020) (7kha) complexes were aligned to Csf RNA (RMSD 5.9 Å, 8.8 Å, and 12.7 Å respectively). Due to the highly curved nature of type I-E (4tvx) (Jackson et al., 2014) and I-F (5uz9) (Chowdhury et al., 2017) crRNA, it was not possible to perform such alignment to IV-B. Instead, individual backbone subunits were aligned to corresponding Csf2 subunits, thus aligning the top of I-E or I-F with the top of IV-B (RMSD ~24.4 Å and 25.8 Å, respectively). In all complexes, non-Cas7/Cas11 subunits are shown as transparent surfaces. All Cas7/Cas11 and RNA, crRNA and TS are colored as in **Figures 1 & 2**, with the addition of the TS in light red. **b**, Alignment of Cas7 with Csf2. Csf2 is shown as grey, transparent cartoon. RMSD is typically ~20 Å – 25 Å, although they clearly align well by eye. The high RMSD is likely due to presence of additional residues not present in Csf2. **c**, Cas11 subunits. All Cas11 subunits are helical bundles that resemble each other. However, due to diverse Cas11 sequences these subunits align poorly (RMSD 16 Å – 18 Å). **d**, Alignment of (cr)RNA from available CRISPR effector complexes. Type IV-B RNA aligns more closely to type III-A and -B crRNAs, consistent with the proposed evolutionary lineage of type IV CRISPR systems emerging from a type III-like ancestor. **e**, Overlay of type IV-B and type III-A CRISPR complexes based on RNA alignment. Type III-A displays the strongest structural homology between Cas7 subunits.

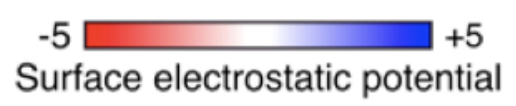
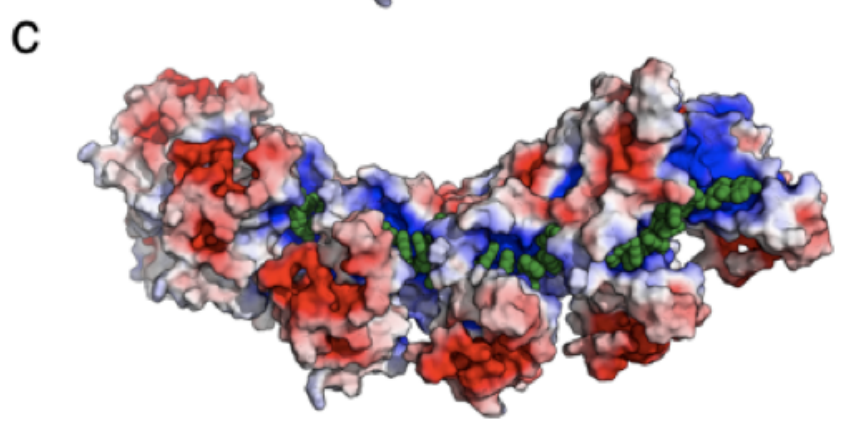
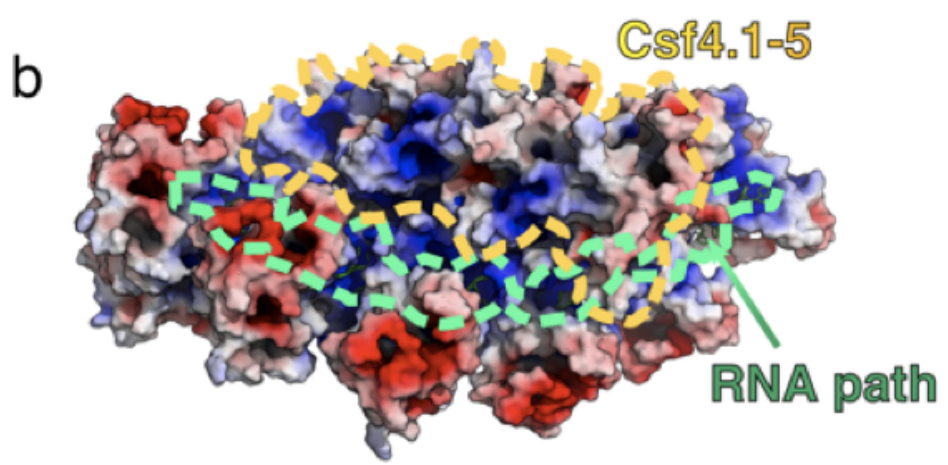
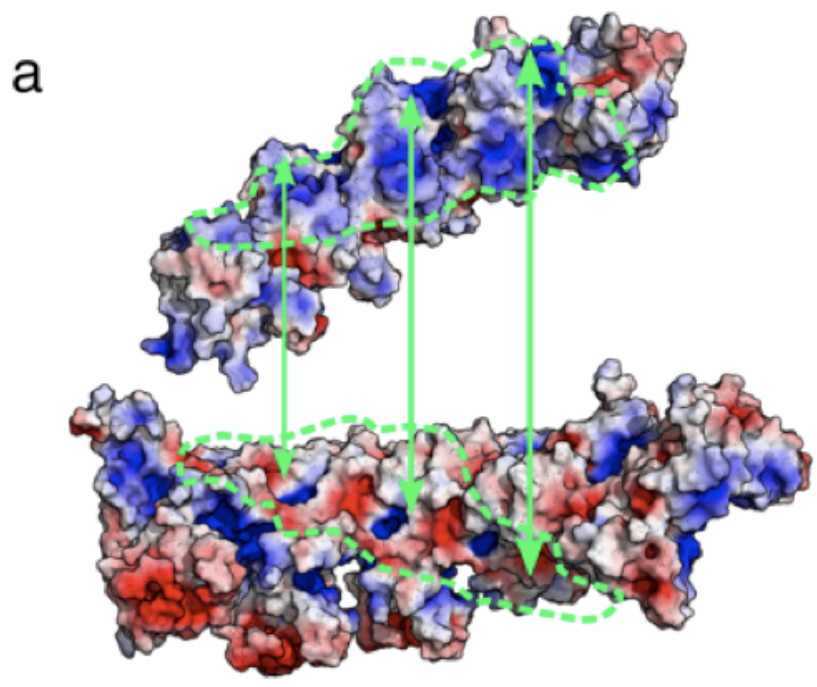


Figure S6. Surface electrostatics of Csf complex. Related to Figure 2. a & b, Cas11 and Csf2 filaments. Green dashed outlines denote complementary surfaces. **b,** Surface electrostatics of the Csf complex. Cas11 subunits and RNA path are outlined. RNA is shown as green cartoon, but it is almost completely occluded by Cas7 subunits. The overall path of the RNA bound within the Cas7 filament is outlined by green dashed lines. **c,** Csf2 filament with RNA contacts (green spheres) shown. Cas11 minor filament is removed for clarity. RNA is bound by a contiguous positively-charged surface. The high electrostatic contribution to RNA binding by Csf2 is typical of non-specific RNA-binding proteins (Bravo et al., 2020, 2018).

Data collection and processing	
Magnification	22,500x
Voltage (kV)	300
Electron exposure (e ⁻ /Å)	40
Defocus range (μM)	-1.5 to -3.0
Symmetry imposed	C1
Final particle images	296,319
Map resolution (Å)	3.9
FSC threshold	0.143
Map resolution range (Å)	3.5 to > 8
Refinement	
Model resolution (Å) (0.143 FSC)	4.1
Map sharpening <i>B</i> factor (Å ²)	130.2
Model composition	
Nonhydrogen atoms	16636
Residues (Protein/RNA)	2083/31
<i>B</i> factors (Å²) (min/max/mean)	
Protein	19.75/206.87/81.59
RNA	34.71/125.88/56.91
r.m.s. deviations	
Bond lengths (Å)/bond angle (°)	0.005/1.112
Validation	
MolProbity score	1.9
Clashscore	4.72
Poor rotamers (%)	0
Ramachandran plot	
Favoured/Allowed/Disallowed (%)	84.99/15.01/0

Table S1. Cryo-EM data collection and processing parameters. Related to Figure 1.

Transparent Methods

Expression and purification of the *M. sp* JS623 Csf complex

E. coli BL21 (DE3) cells containing the pCDF-Duet1-Csf1-Cas11-Strep-Csf2-Csf3(MCS1)-Cas6 array (MCS2) expression vector were inoculated in 6 X 0.5 L lysogeny broth (LB) and grown at 37°C with 200 rpm shaking. Cells were grown to an optical density (O.D. 600 nm) between 0.6-0.7 then cold shocked on ice for 30-60 min. Recombinant protein expression was induced with 0.8 mM IPTG (isopropyl β -D-1-thiogalactopyranoside). After induction, cells were grown at 16°C for 18-24 hours and pelleted via centrifugation. Pelleted cells were resuspended in 20-30 mL Buffer W (100 mM Tris, pH 8.0; 150 mM NaCl; 2 μ M ZnSO₄). Protease inhibitors were added to the following final concentrations: 10 μ g/mL leupeptin, 2 μ g/mL aprotinin, and 170 μ g/mL phenylmethylsulfonyl fluoride (PMSF). Cells were lysed by sonication and lysate was clarified by centrifugation. Polyethylenimine was added to the soluble fraction at a final concentration of 0.1% to precipitate nucleic acids and again clarified by centrifugation. The supernatant was applied to a StrepTrap HP 5 mL column (GE Healthcare) and the bound protein was eluted with Buffer E (Buffer W + 5 mL desthiobiotin). The RNP complex was further purified with a Superose6 Increase 10/300 GL column (GE Healthcare), eluting into SEC Buffer (50 mM HEPES, pH 8.0; 150 mM NaCl; 2 μ M ZnSO₄).

RNA sequencing and analysis

Nucleic acids that co-purified with type IV-B complex were extracted with acid phenol:chloroform and subsequent ethanol precipitation. The resulting fraction was loaded on a 20% denaturing PAGE gel after which a band of approximately 55-60 nt (**Figure S3A**) was excised and purified from gel using the ZR small-RNA PAGE Recovery Kit (Zymo Research, USA). Small RNAs were prepared by GenXPro (GenXPro GmbH, Germany) using the TrueQuant smallRNA Seq kit according to the manufacturer's instructions and were sequenced on a HiSeq2000 (Illumina, USA). After quality control filtering and adapter trimming using Cutadapt (Martin, 2011), the reads were mapped on the expression plasmid and the *E. coli* BL21 (DE3) genome (Genbank accession CP001509) with Geneious Prime 2020.10.2 (<https://www.geneious.com>). For comparing the abundance and processing of (mature) crRNAs of the total cellular RNA population versus those associated with the type IV complex (Figure S2D), the extracted total RNAs (NEB Monarch Total RNA Miniprep Kit) were first depleted for ribosomal RNAs (Invitrogen Ribominus Transcriptome Isolation Kit) before they were sequenced on an Illumina MiSeq (Center for Integrated Biosystems, Utah State University, USA). After quality control and adapter trimming, the resulting reads were mate-paired and merged using SeqPrep (<https://github.com/jstjohn/SeqPrep>), filtered for reads containing CRISPR-array repeat nucleotides, and mapped on the expression plasmid using Geneious (Langmead et al., 2009). Visualisation of the mapping results and further downstream analyses were performed using Geneious and Microsoft Excel.

Cryo-EM data acquisition and processing

C-flat holy carbon grids (CF-4/2, Protochips Inc.) were glow-discharged for 30 seconds using a Gatan Solarus plasma cleaner. 2.5 μ l of Type IV complex (~0.3 mg/ml) was applied onto grids, blotted for 2.5 seconds with a blotting force of 1 and rapidly plunged into liquid ethane using a FEI Vitrobot MarkIV operated at 4 °C and 100% humidity. Data were acquired using a FEI Titan Krios

transmission electron microscope (Sauer Structural Biology Laboratory, University of Texas at Austin) operating at 300 keV at a nominal magnification of $\times 22,500$ (1.1 Å pixel size) with defocus ranging from -1.5 to -3.0 μm . The data were collected using a total exposure of 6 s fractionated into 20 frames (300 ms per frame) with a dose rate of ~ 8 electrons per pixel per second and a total exposure dose of $\sim 40 \text{ e}^- \text{Å}^{-2}$. Three datasets were automatically recorded on a Gatan K2 Summit direct electron detector operated in counting mode using the MSI-Template application within the automated macromolecular microscopy software LEGINON (Suloway et al., 2005).

All image pre-processing was performed in Appion (Lander et al., 2009). Individual movie frames were aligned and averaged using 'MotionCor2' drift-correction software (Zheng et al., 2017). The contrast transfer function (CTF) of each micrograph was estimated using CTFFIND4 (Rohou and Grigorieff, 2015). Particles were picked with a template-based particle picker using a reference-free 2D class average from a small subset of manually picked particles as templates. Selected particles were extracted from micrographs using particle extraction within Relion (Scheres, 2012) and the coordinates exported from Appion. After multiple rounds of 2D classification in Relion to remove junk particles, 824,421 particles were left and imported into cryoSPARC (Punjani et al., 2017) for further processing. After multiple rounds of 2D classification and heterogeneous refinement, a final reconstruction containing 296,319 particles was determined to a global resolution of 3.9 Å (based on the gold standard 0.143 FSC criterion using two independent half-maps) using local refinement (implementing non-uniform refinement) with a mask corresponding to the entire complex.

Csf model building, refinement and structural analysis

An atomic model for the Csf complex was built de novo in Coot (Emsley et al, 2004), and subjected to multiple iterative rounds of molecular dynamics - flexible fitting in Namdinator (Kidmose et al, 2019) and real-space refinement in Phenix (Afonine et al., 2018). The majority of the RNA was modelled as polyU, with occasional bases modelled as A depending on the size of the cryoEM density corresponding to the nucleobase (i.e. if the density was unambiguously a purine, (Bravo et al., 2021)). The refined Csf complex model was validated using MolProbity (Chen et al., 2010) as implemented in Phenix. Protein sequence conservation analysis was performed using online ConSurf (Ashkenazy et al., 2016) server, with multiple sequence alignment (MSA) generated using the top 100 result from a BLAST search against Csf sequences. Output from the MSA was used to generate a sequence logo using the WebLogo server (Crooks et al., 2004). Maps and models were visualized using ChimeraX (Goddard et al., 2018) and the electrostatic surfaces were determined using the APBS plugin (Baker et al., 2001) within PyMol. Root-mean-square deviation (r.m.s.d.) values between equivalent atoms in Csf2 and type III-A Csm3, and between type IV-B RNA and III-A crRNA were calculated using ChimeraX and PyMol.

Supplemental References

- Afonine, P. V., Poon, B.K., Read, R.J., Sobolev, O. V., Terwilliger, T.C., Urzhumtsev, A., Adams, P.D., 2018. Real-space refinement in PHENIX for cryo-EM and crystallography. *Acta Crystallogr. Sect. D Struct. Biol.* 74, 531–544.
- Ashkenazy, H., Abadi, S., Martz, E., Chay, O., Mayrose, I., Pupko, T., Ben-Tal, N., 2016. ConSurf 2016: an improved methodology to estimate and visualize evolutionary conservation in macromolecules. *Nucleic Acids Res.* 44, W344–W350.
- Baker, N.A., Sept, D., Joseph, S., Holst, M.J., McCammon, J.A., 2001. Electrostatics of nanosystems: Application to microtubules and the ribosome. *Proc. Natl. Acad. Sci. U. S. A.* 98, 10037–10041.
- Bravo, J.P.K., Bartnik, K., Venditti, L., Gail, E.H., Davidovich, C., Lamb, D.C., Tuma, R., Calabrese, A.N., Borodavka, A., 2020. Structural basis of rotavirus RNA chaperone displacement and RNA annealing. *bioRxiv* 2020.10.26.354233.
- Bravo, J.P.K., Borodavka, A., Barth, A., Calabrese, A.N., Mojzes, P., Cockburn, J.J.B., Lamb, D.C., Tuma, R., 2018. Stability of local secondary structure determines selectivity of viral RNA chaperones. *Nucleic Acids Res.* 293191.
- Bravo, J.P.K., Dangerfield, T.L., Taylor, D.W., Johnson, K.A., 2021. Remdesivir is a delayed translocation inhibitor of SARS CoV-2 replication. *Mol. Cell.*
- Chen, V.B., Arendall, W.B., Headd, J.J., Keedy, D.A., Immormino, R.M., Kapral, G.J., Murray, L.W., Richardson, J.S., Richardson, D.C., 2010. MolProbity: All-atom structure validation for macromolecular crystallography. *Acta Crystallogr. Sect. D Biol. Crystallogr.* 66, 12–21.
- Chowdhury, S., Carter, J., Rollins, M.C.F., Golden, S.M., Jackson, R.N., Hoffmann, C., Nosaka, L., Bondy-Denomy, J., Maxwell, K.L., Davidson, A.R., Fischer, E.R., Lander, G.C., Wiedenheft, B., 2017. Structure Reveals Mechanisms of Viral Suppressors that Intercept a CRISPR RNA-Guided Surveillance Complex. *Cell* 169, 47-57.e11.
- Crooks, G., Hon, G., Chandonia, J., Brenner, S., 2004. WebLogo: a sequence logo generator. *Genome Res* 14, 1188–1190.
- Goddard, T.D., Huang, C.C., Meng, E.C., Pettersen, E.F., Couch, G.S., Morris, J.H., Ferrin, T.E., 2018. UCSF ChimeraX: Meeting modern challenges in visualization and analysis. *Protein Sci.* 27, 14–25.
- Jackson, R.N., Golden, S.M., van Erp, P.B.G., Carter, J., Westra, E.R., Brouns, S.J.J., van der Oost, J., Terwilliger, T.C., Read, R.J., Wiedenheft, B., 2014. Structural biology. Crystal structure of the CRISPR RNA-guided surveillance complex from *Escherichia coli*. *Science* 345, 1473–1479.
- Jia, N., Mo, C.Y., Wang, C., Eng, E.T., Marraffini, L.A., Patel, D.J., 2019. Type III-A CRISPR-Cas Csm Complexes: Assembly, Periodic RNA Cleavage, DNase Activity Regulation, and Autoimmunity. *Mol. Cell* 73, 264-277.e5.
- Lander, G.C., Stagg, S.M., Voss, N.R., Cheng, A., Fellmann, D., Pulokas, J., Yoshioka, C.,

Irving, C., Mulder, A., Lau, P.W., Lyumkis, D., Potter, C.S., Carragher, B., 2009. Appion: An integrated, database-driven pipeline to facilitate EM image processing. *J. Struct. Biol.* 166, 95–102.

Langmead, B., Trapnell, C., Pop, M., Salzberg, S.L., 2009. Ultrafast and memory-efficient alignment of short DNA sequences to the human genome. *Genome Biol.* 10.

Makarova, K.S., Wolf, Y.I., Iranzo, J., Shmakov, S.A., Alkhnbashi, O.S., Brouns, S.J.J., Charpentier, E., Cheng, D., Haft, D.H., Horvath, P., Moineau, S., Mojica, F.J.M., Scott, D., Shah, S.A., Siksnyš, V., Terns, M.P., Venclovas, Č., White, M.F., Yakunin, A.F., Yan, W., Zhang, F., Garrett, R.A., Backofen, R., van der Oost, J., Barrangou, R., Koonin, E. V., 2020. Evolutionary classification of CRISPR–Cas systems: a burst of class 2 and derived variants. *Nat. Rev. Microbiol.* 18, 67–83.

Martin, M., 2011. Cutadapt removes adapter sequences from high-throughput sequencing reads. *EMBnet.journal* [Online] 17, 10–12.

O'Brien, R.E., Santos, I.C., Wrapp, D., Taylor, D.W., Bravo, J.P.K., Schwartz, E.A., Brodbelt, J.S., 2020. Structural basis for assembly of non-canonical small subunits into type I-C Cascade. *Nat. Commun.* 1–6.

Osawa, T., Inanaga, H., Sato, C., Numata, T., 2015. Crystal structure of the crispr-cas RNA silencing cmr complex bound to a target analog. *Mol. Cell* 58, 418–430.

Punjani, A., Rubinstein, J.L., Fleet, D.J., Brubaker, M.A., 2017. CryoSPARC: Algorithms for rapid unsupervised cryo-EM structure determination. *Nat. Methods* 14, 290–296.

Rohou, A., Grigorieff, N., 2015. CTFFIND4: Fast and accurate defocus estimation from electron micrographs. *J. Struct. Biol.* 192, 216–221.

Scheres, S.H.W., 2012. RELION: Implementation of a Bayesian approach to cryo-EM structure determination. *J. Struct. Biol.* 180, 519–530.

Suloway, C., Pulokas, J., Fellmann, D., Cheng, A., Guerra, F., Quispe, J., Stagg, S., Potter, C.S., Carragher, B., 2005. Automated molecular microscopy: The new Legimon system. *J. Struct. Biol.* 151, 41–60.

Zheng, S.Q., Palovcak, E., Armache, J.P., Verba, K.A., Cheng, Y., Agard, D.A., 2017. MotionCor2: Anisotropic correction of beam-induced motion for improved cryo-electron microscopy. *Nat. Methods* 14, 331–332.